High-wavenumber steady solutions of two-dimensional Rayleigh–Bénard convection between stress-free boundaries

Alexander Takla
Advised by Baole Wen

June 2021

Abstract

Rayleigh–Bénard convection (RBC)—a classical problem in fluid dynamics—plays a significant role in a large range of phenomena in engineering, geophysics and astrophysics, and has been studied extensively to gain insights into the development of turbulence. Recent investigations show that steady solutions share many features with the turbulent RBC from direct numerical simulations and form the state space skeleton of the turbulent dynamics. This study focuses on the high-wavenumber, steady convection roll solutions that bifurcate supercritically from the motionless conductive state for two-dimensional RBC between stress-free boundaries. In order to elucidate the asymptotic behavior of the heat transport enhancement factor, i.e., the Nusselt number Nu, we compute steady convective rolls with aspect ratios $0.06 \leq \Gamma \leq \pi/5$ over six orders of magnitude in the Rayleigh number $10^8 \leq Ra \leq 10^{14}$ for fixed Prandtl number $Pr = 1$. Previous work indicates the dependence of Nu on Γ has a maximum at $\Gamma \approx 1.9$ at large Ra for low and moderate wavenumbers $k = 2\pi/\Gamma \leq 10$ [7]. Preliminary results of this study, however, show that there exists a second *local* maximum in the high-wavernumber regime where the aspect ratio Γ^*_{loc} that locally maximizes $Nu(\Gamma)$ scales as $Ra^{-1/4}$ and the corresponding Nu and Re scale as $Ra^{0.29}$ and $Ra^{2/5}$ respectively as $Ra \to \infty$. Nevertheless, for fixed Γ and as $Ra \to \infty$, our numerical solutions converge back to the Chini-Cox asymptotic solutions [1] with $Nu \sim Ra^{1/3}$ and $Re \sim Pr^{-1}Ra^{2/3}$.

1 Introduction

Convection and conduction are both mechanisms of heat transfer in fluids. In convection, heat transfer is caused by the mass flow of fluid particles, whereas in conduction, it is due to the particles' vibrational motion about their equilibrium. Convection can occur in the presence of an unstable density distribution caused by a negative temperature gradient between its vertical boundaries. For relatively small temperature differences, heat transfer is dominated by conduction and governed by Fourier's Law. However, beyond a critical threshold, convection can no longer be ignored, and heat flux is enhanced.

Determining the enhancing effect of convection has been a central focus in many fields including engineering, geophysics, and astrophysics. Rayleigh-Bénard convection is a minimalistic mathematical model that displays buoyancy-driven convection. This model consists of a fluid contained between two isothermal horizontal boundaries separated by a vertical distance H. The temperature gradient between the two boundaries is negative; the bottom plate is held at a higher temperature than the top in order for convection to occur. Rayleigh-Bénard convection has been diligently studied experimentally, theoretically, and computationally as it remains a relatively simple model to describe a wide variety of complex real-world scenarios.

In Rayleigh-Bénard convection, the measurement of convective heat flux is given by the Nusselt number Nu, defined as the ratio of total heat flux to conductive heat flux. A particular interest in Rayleigh-Bénard convection is determining Nu as a function of the Rayleigh number Ra the ratio of driving to damping forces, the Prandtl number Pr the ratio of momentum diffusivity to thermal diffusivity, and the aspect ratio Γ defined as the domain's width-to-height ratio. Specifically, we are interested in determining Nu as a function of these dimensionless numbers in the asymptotic limit of Ra$\to\infty$.

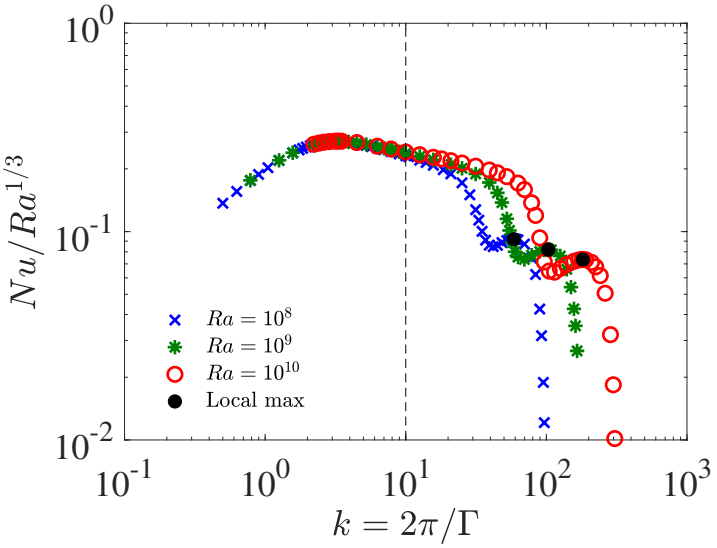

Figure 1: Compensated plot of Nu vs wavenumber $k = 2\pi/\Gamma$ on a log-log plot for stress free steady convection rolls. Smaller wavenumber values, points left of the gray dashed line, were computed by Wen et al. [7]. Recently discovered local-maximum solutions occurred for high-wavenumbers for fixed Ra and Pr, similar to the no slip case [6]. These local maximums are denoted by the black points.

Two theories have been proposed, both predicting a power-law scaling in the turbulent regime, $Nu \sim Pr^{\gamma} Ra^{\beta}$, however varying in the values of γ and β. Classical theory, proposed independently by Priestly [3] and Malkus [2], asserts $Nu \sim Ra^{1/3}$ in the asymptotic regime. Priestly argued that the heat flux should be independent of the vertical distance H between the plates in the turbulent regime for large Γ, and Malkus' maximum dissipation theory also agrees with $\gamma = 0$ and $\beta = 1/3$. Ultimate theory, proposed by Spiegel [4], asserts $Nu \sim Pr^{1/2} Ra^{1/2}$ for $Pr \lesssim 1$. Spiegel augured that heat will be transferred at the fluid's free-fall speed, and thus the heat flux Q will become independent of the kinematic viscosity ν and thermal diffusivity κ.

Asymptotic scaling of the Nusselt number has been studied via direct numerical simulation (DNS) for various boundary conditions and geometries. In the case of steady Rayleigh-Bénard convection with no-slip boundary conditions, the Nusselt number displayed absolute and local maximum features as a function of the domain size Γ for fixed Ra and Pr; and for the optimal choice of Γ, classical 1/3 scaling was achieved [6]. In the case of steady Rayleigh-Bénard convection with stress-free boundary conditions, only an absolute maximum has been observed thus far at $\Gamma \approx 1.9$ for Nusselt as a function of Γ for fixed Ra and Pr [7]. Classical 1/3 scaling was achieved for stress-free boundary conditions $Nu = c(k, Pr) Ra^{1/3}$ for all fixed Γ, and the proportionality prefactor $c(k, Pr)$ was found to be independent of Pr, $c(k, Pr) \to c(k)$ [1]. Predictions of this prefactor were derived by Chini & Cox using the assumption that the plumb's width is negligible compared to the size of the domain. However, we recently discovered that in the case of small Γ, local maximum behavior occurred in the stress-free case, Figure 1, similar to the no-slip case. For high-wavenumber, small Γ, the width of the plumb becomes comparable to the size of the domain, and the assumption made by Chini & Cox is invalid for these domains. Therefore convergence to the Chini & Cox prefactor $c(k)$ remains an open question for high-wavenumber solutions.

This paper investigates the properties of the recently discovered local-maximum solution for the stress-free case and continues the computations done by Wen et al. [7] for higher wavenumbers to test the convergence of these solutions to classical theory and the Chini-Cox prefactor [1]. We performed computations of steady coherent states in nonlinear two-dimensional Rayleigh-Bénard convection with stress-free boundaries using a Newton-GMRES method. Computations were executed over six magnitudes of Ra, $10^8 \leq Ra \leq 10^{14}$ for the local-maximum solution and for fixed aspect ratios $0.06 \leq \Gamma \leq \pi/5$. Our data shows that for the local-maximum solution Nu is proportional to $Ra^{0.29}$, Re is proportional to $Ra^{2/5}$, and Γ is proportional to $Ra^{-1/4}$. For fixed aspect ratios, our results were consistent with classical theory $Nu \sim Ra^{1/3}$ and converged

to the Chini-Cox prefactor; with convergence taking longer for higher wavenumbers $k = 2\pi/\Gamma$. Finally, we found that the width of the plumb scales as $Ra^{-1/3}$ resulting in this width becoming negligible compared to the size of the domain in the limit of $Ra \to \infty$.

The rest of this paper is designed as follows: Section 2 discusses the derivation of the relevant equations used in Rayleigh-Bénard convection, Section 3 contains our computational results, and Section 4 is a discussion of these results and future work.

2 Theoretical background

2.1 Derivation of Navier Stokes Equation

The Navier stokes equation remains one of the most rigorously studied equations in all fluid mechanics due to its wide application to real-world scenarios and its intrinsic mathematical difficulty to solve because of its nonlinearity. The Navier stokes equation is a set of coupled nonlinear partial differential equations that govern the motion of all Newtonian fluids. These equations can be derived using the Reynolds transport theorem,

$$\frac{\partial}{\partial t}\int_V \rho b dV + \int_S \rho b \mathbf{u}\cdot\hat{n}dA = \frac{DB}{Dt}, \tag{2.1}$$

which relates an extensive property B, a properties proportional to mass, to an intensive property $b = B/m$. The continuity equation can be derived by setting $B = m$ and recognizing that the right side of the equation goes to zero from conservation of mass.

$$\begin{aligned}
\frac{\partial}{\partial t}\int_V \rho dV + \int_S \rho\mathbf{u}\cdot\hat{n}dA &= 0,\\
\frac{\partial}{\partial t}\int_V \rho dV + \int_V \nabla\cdot(\rho\mathbf{u})dV &= 0,\\
\frac{\partial\rho}{\partial t} + \nabla\cdot(\rho\mathbf{u}) &= 0.
\end{aligned} \tag{2.2}$$

We transformed the surface integral to a volume integral by use of the divergence theorem and took the limit as $V \to 0$ to get Eq. 2.2, the continuity equation. The conservation of momentum equation can be derive similarly by setting $B = m\mathbf{u}$ and recognizing the right side as the time rate of change of momentum which by Newton's second law is equal to the sum of the forces.

$$\begin{aligned}
\frac{\partial}{\partial t}\int_V \rho\mathbf{u}dV + \int_S \rho\mathbf{u}(\mathbf{u}\cdot\hat{n})dA &= -\int_S P\hat{n}dA + \int_S \mu\nabla\mathbf{u}dA + \int_V \rho\mathbf{g}dV,\\
\frac{\partial}{\partial t}\int_V \rho\mathbf{u}dV + \int_V \nabla\cdot(\rho\mathbf{u}\mathbf{u})dV &= -\int_V \nabla P dV + \int_V \mu\nabla\cdot\nabla\mathbf{u}dA + \int_V \rho\mathbf{g}dV,\\
\rho\left(\frac{\partial\mathbf{u}}{\partial t} + \mathbf{u}\cdot\nabla\mathbf{u}\right) + \mathbf{u}\cancel{\left(\frac{\partial\rho}{\partial t} + \nabla\cdot(\mathbf{u}\rho)\right)} &= -\nabla P + \mu\nabla^2\mathbf{u} + \rho\mathbf{g},\\
\rho\left(\frac{\partial\mathbf{u}}{\partial t} + \mathbf{u}\cdot\nabla\mathbf{u}\right) &= -\nabla P + \mu\nabla^2\mathbf{u} + \rho\mathbf{g}.
\end{aligned} \tag{2.3}$$

We transformed the surface integrals to volume integrals by use of the divergence theorem and took the limit as V $\to 0$ to get Eq. 2.3, the momentum equation. The $\frac{\partial\rho}{\partial t} + \nabla\cdot(\mathbf{u}\rho)$ term cancels out due to Eq. 2.2. The continuity equation, Eq. 2.2, and the momentum equation, Eq. 2.3, make up the Navier stokes equations

$$\frac{\partial\rho}{\partial t} + \nabla\cdot(\rho\mathbf{u}) = 0, \tag{2.4a}$$

$$\rho\left(\frac{\partial\mathbf{u}}{\partial t} + \mathbf{u}\cdot\nabla\mathbf{u}\right) = -\nabla P + \mu\nabla^2\mathbf{u} + \rho\mathbf{g}. \tag{2.4b}$$

Where $\mathbf{u}$, the velocity field, P, the pressure, and ρ, the density, are in general functions of position and time.

2.2 Application of Navier Stokes to Rayleigh-Bénard convection

Rayleigh-Bénard convection is the natural convection that occurs due to an unstable density distribution arising from a negative temperature gradient. To describe this phenomenon, we need the Navier Stokes equations that govern the fluid's motion, the diffusive equation, which represents how the temperature evolves, and an equation to measure the density variations. In our problem, we assumed that the density takes on the following form $\rho = \rho_o(1-\alpha(T-T_o))$ and applied the Boussinesq approximation; the variation in density is only relevant in the buoyancy gravity term. The relevant equations in dimensionless form become,

$$\frac{\partial \mathbf{u}}{\partial t} + \mathbf{u}\cdot\nabla\mathbf{u} = -\nabla P + Pr\nabla^2\mathbf{u} + PrRaT\hat{z}, \tag{2.5a}$$

$$\nabla\cdot\mathbf{u} = 0, \tag{2.5b}$$

$$\frac{\partial T}{\partial t} + \mathbf{u}\cdot\nabla\mathbf{T} = \nabla^2 T. \tag{2.5c}$$

The equations have been nondimensionalized in terms of the separation distance between the boundaries H, the thermal diffusion time $\frac{H^2}{\kappa}$ where κ is the thermal diffusivity, and the temperature drop ΔT between the bottom and top boundaries. In this paper, we consider the steady solution, so naturally all time derivatives go to zero and $\mathbf{u} = u\hat{x} + w\hat{z}$ the velocity field, P the pressure, and T the temperature are functions of x and z

The relevant dimensionless numbers in Eq. 2.5 are the Rayleigh number $Ra = \frac{g\alpha\Delta T H^3}{\kappa\nu}$ where g is the gravitational acceleration, α is the thermal expansion coefficient, and ν is the kinematic viscosity, the Prandtl number $Pr = \frac{\nu}{\kappa}$, and the aspect ratio Γ the width-to-height ratio of the domain in our problem. The dimensionless spatial domain for our problem is $(x,z) \in [0,\Gamma]\times[0,1]$ where the width of one roll is $\frac{\Gamma}{2}$. At the top and bottom boundaries, the temperature field satisfies isothermal boundary conditions, and the velocity field satisfies no-penetration and stress-free boundary conditions.

$$T|_{z=0} = 1, \qquad T|_{z=1} = 0, \qquad w|_{z=0,1} = 0, \qquad \partial_z u|_{z=0,1} = 0. \tag{2.5d}$$

From the solutions of Eq. 2.5, the Nusselt number $Nu = \frac{QH}{\rho c\kappa\Delta T}$, where Q is the total heat flux and c is the specific heat, and the Reynolds number $Re = \frac{U_{rms}H}{\nu}$, where U_{rms} is the root-mean-squared velocity, can be calculated by the following equations.

$$Nu = 1 + \langle wT\rangle, \tag{2.6}$$

$$Re = 1 + \langle u^2 + w^2\rangle^{1/2}. \tag{2.7}$$

From classical theory, we expect that as $Ra\to\infty$, $Nu \sim Ra^{1/3}$ and $Re \sim Pr^{-1}Ra^{2/3}$ where the constant of proportionality depends on the choice of Γ.

2.3 Stream function-vorticity formulation

We made use of a vorticity-stream function in order to simplify Eq. 2.5. The stream function Ψ can be defined for any two-dimensional incompressible flow. The stream function can be used to plot streamlines, representing the trajectories of particles in a steady flow and inherently satisfy the continuity equation, Eq. 2.5b. In general, we can define the stream function $\mathbf{\Psi}$ as

$$\mathbf{u} = \nabla\times\mathbf{\Psi}, \tag{2.8}$$

but since our velocity is two dimensional in x and z, this simply reduces to

$$\mathbf{u} = \frac{\partial\Psi}{\partial z}\hat{x} - \frac{\partial\Psi}{\partial x}\hat{z}. \tag{2.9}$$

On direct substitution it is clear that Eq. 2.9 satisfies the continuity equation,

$$\nabla\cdot\left(\frac{\partial\Psi}{\partial z}\hat{x} - \frac{\partial\Psi}{\partial x}\hat{z}\right) = 0,$$

$$\frac{\partial}{\partial x}\left(\frac{\partial \Psi}{\partial z}\right) - \frac{\partial}{\partial z}\left(\frac{\partial \Psi}{\partial x}\right) = 0.$$

Interchanging the order of differentiation by the symmetry of the second partial derivative,

$$\cancel{\frac{\partial}{\partial z}\left(\frac{\partial \Psi}{\partial x}\right)} - \cancel{\frac{\partial}{\partial z}\left(\frac{\partial \Psi}{\partial x}\right)} = 0.$$

Introducing the stream function provides a meaningful simplification since it allows us to deal with one unknown Ψ rather than two unknowns u and w.

The vorticity field $\boldsymbol{\omega}$ describes the rotational motion of the fluid at every position. Mathematically, vorticity is defined as the curl of the velocity field,

$$\boldsymbol{\omega} = \nabla \times \mathbf{u}. \tag{2.10}$$

In two-dimensional flow, the vorticity vector field reduces to a scalar field since $\boldsymbol{\omega}$ is always perpendicular to the plane of the flow, the y-direction in our model. For two dimensional flow, the negative vorticity scalar can be written as,

$$\omega = \frac{\partial w}{\partial x} - \frac{\partial u}{\partial z}. \tag{2.11}$$

For two-dimensional steady incompressible flow, we can represent the Naiver Stokes equations and the diffusion equation in terms of the stream function Ψ and the vorticity ω. The motivation for this is that by introducing Ψ we do not have to solve for individual velocity components, and by introducing ω it allows us to combine the x and z component of Eq. 2.5a into one, reducing the number of equations that we need to solve. To maintain Dirichlet boundary conditions, we introduce θ defined as the deviation of the temperature field T from the conduction profile $1 - z$. What follows is a derivation of Eq. 2.5 in terms of Ψ, ω, and θ.

Since the stream function naturally satisfies the continuity equation, we need to obtain a third equation that relates Ψ, ω, and θ. From Eq. 2.10, there is a relationship between ω and the components of the velocity. However we know that $u = \frac{\partial \Psi}{\partial z}$ and $w = -\frac{\partial \Psi}{\partial x}$. Upon direct substitution into Eq. 2.10, we obtain

$$\omega = -\nabla^2 \Psi. \tag{2.12}$$

Eq. 2.5a in it x and z components is

$$u\frac{\partial u}{\partial x} + w\frac{\partial u}{\partial z} = -\frac{\partial P}{\partial x} + Pr\left(\frac{\partial^2 u}{\partial x^2} + \frac{\partial^2 u}{\partial z^2}\right), \tag{2.13a}$$

$$u\frac{\partial w}{\partial x} + w\frac{\partial w}{\partial z} = -\frac{\partial P}{\partial z} + Pr\left(\frac{\partial^2 w}{\partial x^2} + \frac{\partial^2 w}{\partial z^2}\right) + PrRa(\theta - z + 1). \tag{2.13b}$$

Take Eq. 2.13a partial derivative with respect to z and take Eq. 2.13b partial derivative with respect to x,

$$\frac{\partial u}{\partial z}\frac{\partial u}{\partial x} + u\frac{\partial^2 u}{\partial z \partial x} + \frac{\partial w}{\partial z}\frac{\partial u}{\partial z} + w\frac{\partial^2 u}{\partial z^2} = -\frac{\partial^2 P}{\partial z \partial x} + Pr\left(\frac{\partial^2}{\partial x^2}\left(\frac{\partial u}{\partial z}\right) + \frac{\partial^2}{\partial z^2}\left(\frac{\partial u}{\partial z}\right)\right), \tag{2.14a}$$

$$\frac{\partial u}{\partial x}\frac{\partial w}{\partial x} + u\frac{\partial^2 w}{\partial x^2} + \frac{\partial w}{\partial x}\frac{\partial w}{\partial z} + w\frac{\partial^2 w}{\partial x \partial z} = -\frac{\partial^2 P}{\partial x \partial z} + Pr\left(\frac{\partial^2}{\partial x^2}\left(\frac{\partial w}{\partial x}\right) + \frac{\partial^2}{\partial z^2}\left(\frac{\partial w}{\partial x}\right)\right) + PrRa\frac{\partial \theta}{\partial x}. \tag{2.14b}$$

Now take Eq. 2.14b and subtract Eq. 2.14a along with using the definition of Ψ and ω to obtain

$$\frac{\partial \Psi}{\partial z}\frac{\partial \omega}{\partial x} - \frac{\partial \Psi}{\partial x}\frac{\partial \omega}{\partial z} = Pr\nabla^2 \omega + PrRa\frac{\partial \theta}{\partial x}. \tag{2.15}$$

Eq. 2.5c in terms of Ψ, ω, and θ is simply

$$\frac{\partial \Psi}{\partial z}\frac{\partial \theta}{\partial x} - \frac{\partial \Psi}{\partial x}\frac{\partial \theta}{\partial z} = -\frac{\partial \Psi}{\partial x} + \nabla^2 \theta. \tag{2.16}$$

So the governing equations for our problem become

$$\frac{\partial \Psi}{\partial z}\frac{\partial \omega}{\partial x} - \frac{\partial \Psi}{\partial x}\frac{\partial \omega}{\partial z} = Pr\nabla^2\omega + PrRa\frac{\partial \theta}{\partial x}, \tag{2.17a}$$

$$\nabla^2\Psi = -\omega, \tag{2.17b}$$

$$\frac{\partial \Psi}{\partial z}\frac{\partial \theta}{\partial x} - \frac{\partial \Psi}{\partial x}\frac{\partial \theta}{\partial z} = -\frac{\partial \Psi}{\partial x} + \nabla^2\theta. \tag{2.17c}$$

Satisfying Dirichlet boundary conditions,

$$\Psi|_{z=0,1} = 0, \qquad \omega|_{z=0,1} = 0, \qquad \theta|_{z=0,1} = 0. \tag{2.17d}$$

2.4 Numerical Method

Eq. 2.17 cannot be solved analytically, so we need to take advantage of computational methods to solve this system of partial differential equations. The method used in our paper was a Newton–GMRES (generalized minimal residual) iterative scheme. The residuals of Eq. 2.17 are

$$F^{\omega}_{res} = Pr\nabla^2\omega + PrRa\frac{\partial \theta}{\partial x} - \frac{\partial \Psi}{\partial z}\frac{\partial \omega}{\partial x} + \frac{\partial \Psi}{\partial x}\frac{\partial \omega}{\partial z}, \tag{2.18a}$$

$$F^{\Psi}_{res} = \nabla^2\Psi + \omega, \tag{2.18b}$$

$$F^{\theta}_{res} = \nabla^2\theta - \frac{\partial \Psi}{\partial z}\frac{\partial \theta}{\partial x} + \frac{\partial \Psi}{\partial x}\frac{\partial \theta}{\partial z} - \frac{\partial \Psi}{\partial x}. \tag{2.18c}$$

To minimize the residuals, we start by choosing an initial guess for Ψ, ω, and θ denoted $(\Psi^0, \omega^0, \theta^0)$. Corrections are made to $(\Psi^0, \omega^0, \theta^0)$ until we obtain a solution to Eq. 2.17. To acquire the ith correction, $(\Delta^{\Psi_i}, \Delta^{\omega_i}, \Delta^{\theta_i})$, we solve the following Jacobian matrix problem:

$$\left(Pr\nabla^2 - \frac{\partial \Psi}{\partial z}\frac{\partial}{\partial x} + \frac{\partial \Psi}{\partial x}\frac{\partial}{\partial z}\right)^i \Delta^{\omega_i} + \left(-\frac{\partial \omega}{\partial x}\frac{\partial}{\partial z} + \frac{\partial \omega}{\partial z}\frac{\partial}{\partial x}\right)^i \Delta^{\Psi_i} + RaPr\frac{\partial}{\partial x}\Delta^{\theta_i} = -{F^{\omega}_{res}}^i, \tag{2.19a}$$

$$\Delta^{\omega_i} + \nabla^2\Delta^{\Psi_i} = -{F^{\Psi}_{res}}^i, \tag{2.19b}$$

$$\left(-\frac{\partial}{\partial x} + \frac{\partial \theta}{\partial z}\frac{\partial}{\partial x} - \frac{\partial \theta}{\partial x}\frac{\partial}{\partial z}\right)^i \Delta^{\Psi_i} + \left(\nabla^2 - \frac{\partial \Psi}{\partial z}\frac{\partial}{\partial x} + \frac{\partial \Psi}{\partial x}\frac{\partial}{\partial z}\right)^i \Delta^{\theta_i} = -{F^{\theta}_{res}}^i, \tag{2.19c}$$

for each ith Newton iteration. The ith corrections are defined as

$$\Delta^{\Psi_i} = \Psi^{i+1} - \Psi^i, \qquad \Delta^{\omega_i} = \omega^{i+1} - \omega^i, \qquad \Delta^{\theta_i} = \theta^{i+1} - \theta^i. \tag{2.20}$$

Newton iterations are continued until proper convergence has occurred and no more meaningful corrections can be made to $(\Psi^0, \omega^0, \theta^0)$; corresponding to the magnitude of the residuals approaching zero. At this point, when $F^{\Psi,\omega,\theta}_{res} \to 0$, we have obtained a solution to Eq. 2.17. Since Eq. 2.19b is linear, we simply solve it by setting ${F^{\Psi}_{res}}^i = 0$ resulting in the following Poisson Equation, $\nabla^2\Delta^{\Psi_i} = -\Delta^{\omega_i}$, which can be solved directly for Δ^{Ψ_i} for a given Δ^{ω_i}. At this point Eq. 2.19a and Eq. 2.19c can be solved simultaneously for Δ^{ω_i} and Δ^{θ_i}

For each Newton iteration, Eq. 2.19 is solved for Δ^{ω_i} and Δ^{θ_i} using the GMRES method with the partial derivatives computed by the spectral method. The spatial discretization is spectral, using a Fourier series in x and a Chebyshev collocation method in z [5]. We simplify computations by solving the problem on one-quarter of the domain as the solutions have centro-reflection symmetry.

$$[\omega, \Psi, \theta](x, z) = [\omega, \Psi, -\theta](\Gamma/2 - x, 1 - z), \qquad [\omega, \Psi, \theta](x, z) = [-\omega, -\Psi, \theta](\Gamma - x, z). \tag{2.21}$$

GMRES iterations are continued until the relative residual error is less than 10^{-2} and Newton iteration are continued until $|F_{res}| < 10^{-10}$. Solutions were first computed for smaller Ra, and for larger Ra, results from smaller Ra were used as the initial guess.

3 Results

We computed steady rolls solutions for moderate to large Ra values ranging from $10^8 \leq Ra \leq 10^{14}$. Solutions were calculated for the newfound Γ^*_{loc}, the value which locally maximize Nu when Ra and Pr are fixed, and for fixed aspect ratio $\Gamma = 0.06, 0.08, 0.1, 0.2, 0.4, 0.5, \pi/5$ continuing where Wen et al. [7] left off. Our results are divided into two sections; local maximum properties and results for fixed Γ.

3.1 Local-maximum solution

The local-maximum solution displayed the following scaling of the Nusselt number, Reynolds number, and the wavenumber as functions of the Rayleigh number in the asymptotic regime.

$$Nu \sim Ra^{0.29}, \quad Re \sim Ra^{2/5}, \quad \text{and} \quad k \sim Ra^{1/4} \quad \text{as} \quad Ra \to \infty \tag{3.1}$$

These findings are consistent with the no-slip case Wen et al. [6].

Figure 2 shows the dimensionless temperature, stream function, and vorticity fields from left to right. These fields have an aspect ratio of $\Gamma = \Gamma^*_{loc} \approx 0.0063$ and were calculate for $Ra = 10^{13}$ and $Pr = 1$. All of these fields have centro-reflection symmetries (see Eq. 2.21), and the interior has an analytical solution; however, not satisfying the boundary conditions,

$$T = -A\sqrt{Pr/Ra}k^3 \cos kx + 1/2(k^4/Ra + 1) - k^4/Raz, \tag{3.2a}$$

$$\Psi = A\sqrt{PrRa} \sin kx, \tag{3.2b}$$

$$\omega = Ak^2\sqrt{PrRa} \sin kx. \tag{3.2c}$$

The panel to the left shows the dimensionless temperature field T where redder regions represent hotter temperatures. This panel clear exhibits a negative temperature gradient in the z-direction and the x-direction about the line $x = \Gamma/2$. The temperature at the boundaries is given by the isothermal boundary conditions $T|_{z=0} = 1$ and $T|_{z=1} = 0$ resulting in a rapid change of the field there. What is of particular interest is the similarity of the inner contour lines to a sinusoidal function. This is expected from the analytical solution valid for the interior since we can rearrange Eq. 3.2a for a fixed temperature T_o and obtain $A' \cos kx + C(T_o) = z$ where $C(T_o)$ and A' are simply constants. This approximation for the contour lines is valid for medial values of the temperature, $0.47 \leq T_o \leq 0.53$. Beyond these values of T_o a sinusoidal fit is impractical as can be seen by the contour lines in the upper corners and bottom middle. The middle panel depicts the stream function with larger positive quantities associated with redder regions. The stream function is maximized at two values ($\Gamma/4$, 2/33) and ($\Gamma/4$, 31/33) and is minimized at ($3\Gamma/4$, 2/33) and ($3\Gamma/4$, 31/33). The vertical boundaries satisfy Dirichlet boundary conditions, so $\Psi|_{z=0,1} = 0$ resulting in a dramatic change of Ψ near the boundaries. In the horizontal direction, the field gradually changes between values, and there are three lines where Ψ is zero, $\Psi_{x=0,\Gamma/2,\Gamma} = 0$. The bulk of the interior satisfies a z-independent sinusoidal function relating x and T given by Eq. 3.2b. This analytical solution is valid for most z-values, $0.2 \leq z \leq 0.8$. Beyond these values, especially near the vertical boundaries, the stream function no longer exhibits z-independence, which is easily seen near the extreme values of Ψ. The vorticity function is illustrated on the right panel with larger positive quantities associated with redder regions. The vorticity function also exhibits multi-extremum features similar to the stream function however with the x-values of each maximum and each minimum deviating slightly. The vorticity function takes on its maximum value at two points, ($15\Gamma/64$, 15/16) and ($17\Gamma/64$, 1/16) and obtains its minimum values at ($47\Gamma/64$, 1/16) and ($49\Gamma/64$, 15/16). The vertical boundaries are fixed at a value of zero $\omega|_{z=0,1} = 0$ causing a sudden change in the vorticity field there. As in the stream function, the field gradually changes along the horizontal direction, and there are three lines where ω is zero, $\omega_{x=0,\Gamma/2,\Gamma} = 0$. A z-independent sinusoidal function similar to the stream function, with an additional factor of k^2, is valid for the interior of the vorticity function. Eq. 3.2c is accurate for most of the interior, specifically for $0.2 \leq z \leq 0.8$; However, the analytical solution breaks down for z-values beyond this range as a result of satisfying the boundary conditions.

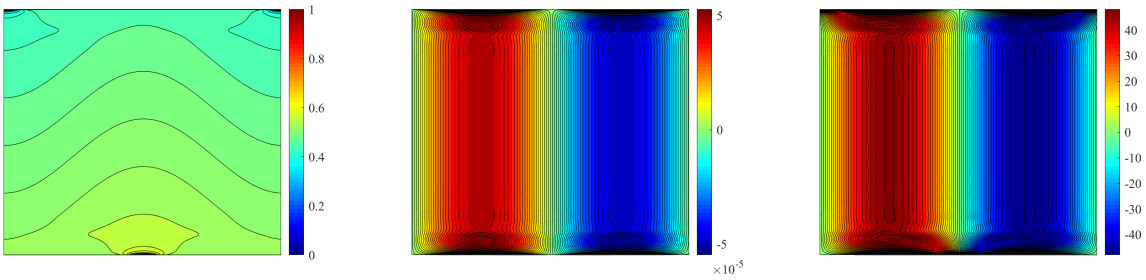

Figure 2: Contours of temperature, stream function, and vorticity fields, from left to right, for $Ra = 10^{13}$, $Pr = 1$, and $\Gamma = \Gamma^*_{loc}$. Color represents the values of the dimensionless variables T, Ψ and ω; smaller values are associated with the color blue, neutral values with green, and larger values with red. The aspect ratio of these images is intentionally much larger than the aspect ratio of the problem, $\Gamma^*_{loc} \approx 0.0063$, in order to magnify the finer details of these scalar fields. Locations that appear black represent a rapid change of the field. Notable these rapid changes occur at the vertical boundaries.

The Ra-dependence of the Nusselt number for Γ^*_{loc} is illustrated in the left panel of Figure 3 for $Pr = 1$. Data fitting over the last decade of Rayleigh numbers $10^{13} \leq Ra \leq 10^{14}$ to a power-law relationship of the form $Nu = CRa^{\beta_n}$ yielded a constant of proportionality of $C = 0.1962$ and an exponent value of $\beta_n = 0.2902$. This 0.29 Ra-scaling of the Nusselt number is consistent with the properties of the local-maximum solution in 2D steady RBC with no-slip boundary conditions [6]. The values of the local exponent $\beta_n = \frac{d\log(Nu)}{d\log(Ra)}$ as a function of Ra is shown in the right panel of Figure 3. Convergence to 0.29 occurred from below, and the value of the local exponent slightly surpasses 0.29 when $Ra \geq 10^{27/2}$.

The left panel of Figure 4 shows the relationship between the Reynolds number and the Rayleigh number for Γ^*_{loc} and $Pr = 1$. Data fitting over the last decade of Rayleigh numbers $10^{13} \leq Ra \leq 10^{14}$ to a function of the form $Re = CRa^{\beta_r}$ gave values of $C = 0.736$ and $\beta_r = 0.3971$. This value of the exponent $\beta_r \approx 2/5$ is consistent with the findings for the local-maximum solution in no-slip steady 2D RBC where 2/5 Ra-scaling of the Reynolds number occurred [6]. The right panel of Figure 4 shows the local exponent $\beta_r = \frac{d\log(Re)}{d\log(Ra)}$ for moderate to high Ra-values. Our data is concentrated around $\beta_r = 2/5$ with a minimal decreasing trend for $10^{42/4} \leq Ra \leq 10^{55/4}$ and a slight increase when $Ra = 10^{14}$.

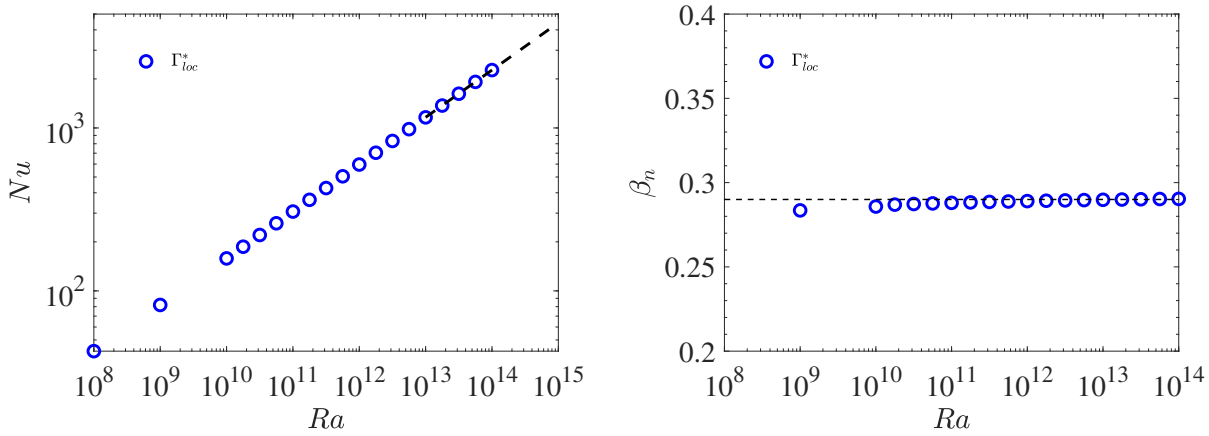

Figure 3: Left: Nu dependence on Ra for steady rolls on a log-log plot for local-maximum solutions with $Pr = 1$. The dashed line is the asymptotic power law relationship between Nu and Ra fitted to the last decade of data, $Nu = 0.1962Ra^{0.2902}$. Right: Finite difference approximation of the local exponent $\beta_n = \log(Nu_{i+1}/Nu_i)/\log(Ra_{i+1}/Ra_i)$ vs. Ra on a semi-log plot for steady rolls with $Pr = 1$ and $\Gamma = \Gamma^*_{loc}$. A local exponent of 0.29 is denoted by the black dashed line.

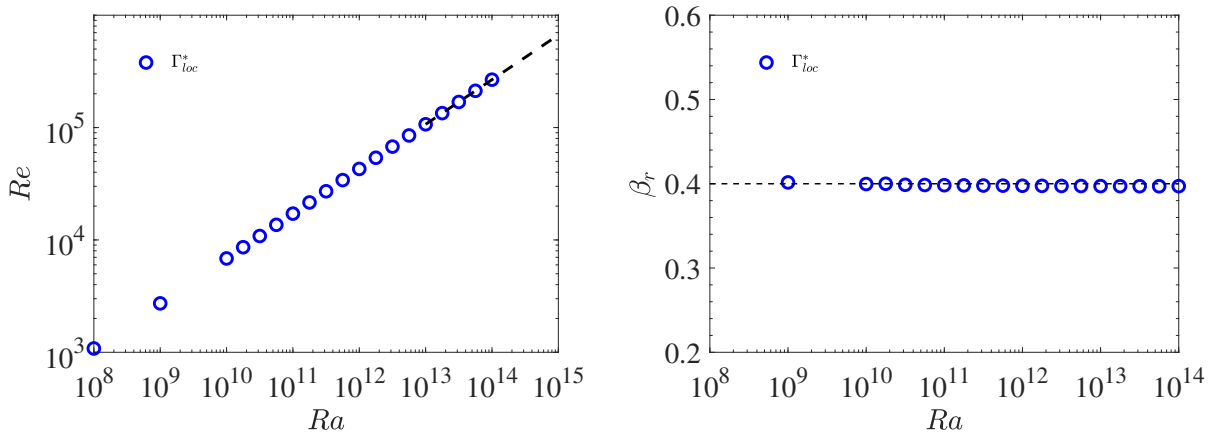

Figure 4: Left: Re dependence on Ra for steady rolls on a log-log plot for local-maximum solutions with $Pr = 1$. The dashed line is the asymptotic power law relationship between Nu and Ra fitted to the last decade of data, $Nu = 0.736Ra^{0.3971}$. Right: Finite difference approximation of the local exponent $\beta_r = \log(Re_{i+1}/Re_i)/\log(Ra_{i+1}/Ra_i)$ vs. Ra on a semi-log plot for steady rolls with $Pr = 1$ and $\Gamma = \Gamma^*_{loc}$. A local exponent of 2/5 is denoted by the black dashed line.

The wavenumber-Rayleigh relationship is plotted in the left panel of Figure 5 for Γ^*_{loc} and $Pr = 1$. A power-law relationship between k and Ra of the form $k = CRa^{\beta_k}$ was calculated over the last decade of the Rayleigh number, $10^{13} \leq Ra \leq 10^{14}$ producing values $C = 0.5902$ and $\beta_k = 0.2485$. The value of the exponent in the stress-free case $\beta_k \approx 1/4$ is consistent with $1/4$ Ra-scaling of the local maximum wavenumber demonstrated in no-slip steady 2D RBC [6]. Convergence of the local exponent $\beta_k = \frac{d\log(k)}{d\log(Ra)}$ to $1/4$ is illustrated in the right panel of Figure 5. The local exponent β_k approaches $1/4$ from below reaching its peak value of $\beta_k \approx 0.2485$ at $Ra = 10^{55/4}$. The increasing trend of our data suggests that β_k will continue to asymptotically increases towards $1/4$ for sufficiently large Ra-values.

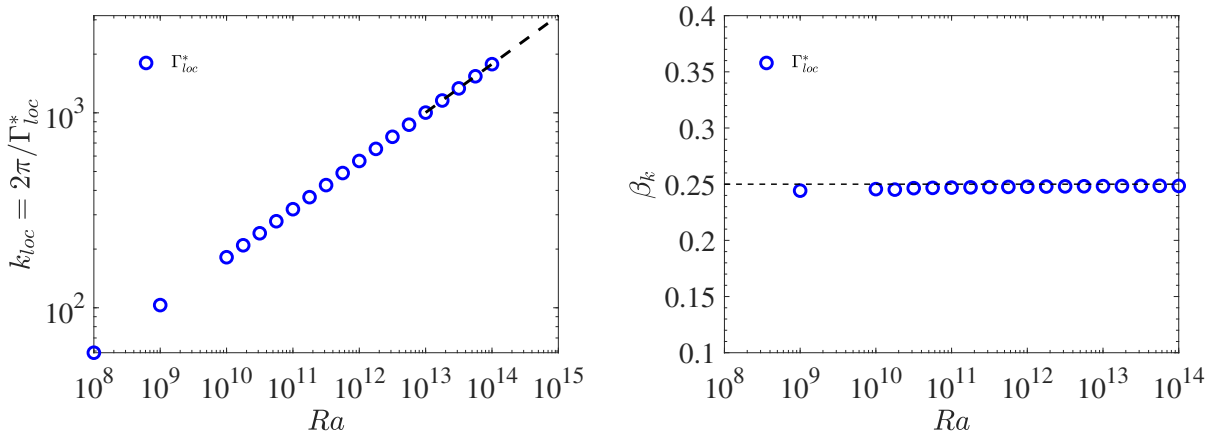

Figure 5: Left: k_{loc} dependence on Ra for steady rolls on a log-log plot for local-maximum solutions with $Pr = 1$. The dashed line is the asymptotic power law relationship between k_{loc} and Ra fitted to the data, $k_{loc} = 0.5902Ra^{0.2485}$. Right: Finite difference approximation of the local exponent $\beta_k = \log(k_{i+1}/k_i)/\log(Ra_{i+1}/Ra_i)$ vs. Ra on a semi-log plot for steady rolls with $Pr = 1$ and $\Gamma = \Gamma^*_{loc}$. A local exponent of $1/4$ is denoted by the black dashed line.

3.2 Fixed-Γ solutions

For sufficiently large Ra, our data for fixed high-wavenumber $k = 2\pi/\Gamma$ agreed with classical theory,

$$Nu = c_n(k)Ra^{1/3} \quad \text{and} \quad Re = c_r(k)Pr^{-1}Ra^{2/3} \quad \text{as} \quad Ra \to \infty \tag{3.3}$$

Both of these scalings are consistent with the asymptotic behavior predicted by Chini & Cox [1]. Asymptotic approximations of the stream function and vorticity function provided an expressions for $c_n(k)$ and $c_r(k)$, derived in terms of $c_n(k)$, Wen et al. [7].

Figure 6 shows the dimensionless temperature, stream function, and vorticity fields from left to right. These fields have an aspect ratio of $\Gamma = 0.1$ and were calculate for $Ra = 10^{13}$ and $Pr = 1$. All of these fields have centro-reflection symmetries (see Eq. 2.21). The left panel illustrates the temperature field with hotter temperatures represented by the color red. As we can see, the temperature field develops an isothermal core with a value of 0.5 for nearly all values besides points on or extremely close to the vertical and horizontal boundaries. This is quite different than the local maximum case in which the interior is not a constant. At the vertical boundaries, the temperature is determined by the boundary conditions $T|_{z=0} = 1$ and $T|_{z=1} = 0$ resulting in a rapid change of the temperature there. At the left and right boundaries, where $x = 0$ and $x = \Gamma$, the temperature is lower than the isothermal core, and when $x = \Gamma/2$, the temperature is larger. This is as expected by the counter-rotating steady convective rolls we are studying. The middle panel represents the stream function with larger positive quantities associated with redder regions. Unlike the local maximum's stream function, this field does not exhibit multi-extremum features and has a maximum at $(\Gamma/4,\ 1/2)$ and a minimum at $(3\Gamma/4,\ 1/2)$. The values of Ψ at the vertical boundaries are identically zero given by the boundary conditions $\Psi|_{z=0,1} = 0$ and transition to these boundary conditions occur very quickly. In the horizontal direction, we see no abrupt transition between values and $\Psi_{x=0,\Gamma/2,\Gamma} = 0$. The right panel shows the vorticity field with larger values associated with redder regions. As illustrated in this panel, nearly all values left of $\Gamma/2$, except points near the perimeter, take on a constant positive value $\Psi_L \approx 67.36$. Similarly, all values right of $\Gamma/2$, except points near the perimeter, take on a constant negative value of the same magnitude $\Psi_R \approx -67.36$. This is very different than the vorticity of the local maximum where there was a gradual transition in the horizontal direction. The boundary conditions $\omega|_{z=0,1} = 0$ result in a aggressive change of the vorticity field near these values. Similarly, along the left, middle, and right boundaries, the vorticity suddenly collapses to zero, that is $\omega|_{x=0,\Gamma/2,\Gamma} = 0$.

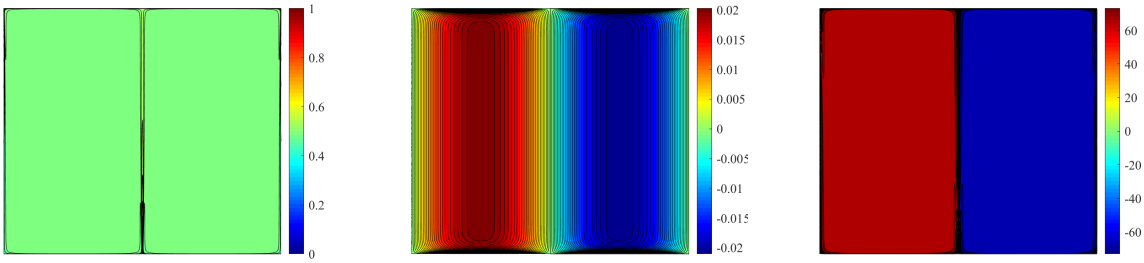

Figure 6: Contours of temperature, stream function, and vorticity fields, from left to right, for $Ra = 10^{13}$, $Pr = 1$, and $\Gamma = 0.1$. Color represents the values of the dimensionless variables T, Ψ and ω; smaller values are associated with the color blue, neutral values with green, and larger values with red. The aspect ratio of these images is intentionally much larger than the aspect ratio of the problem, $\Gamma = 0.1$, in order to magnify the finer details of these scalar fields. Locations that appear black represent a rapid change of the field. Notable these rapid changes occur at the vertical and horizontal boundaries and at the horizontal mid-line

Figure 7 shows the compensated Nusselt number $Nu/Ra^{1/3}$ and the local exponent β_n as functions of the Rayleigh number over a variety of aspect ratios with $Pr = 1$. In the graph of $Nu/Ra^{1/3}$ vs Ra, the compensated Nusselt number approaches a different horizontal line depending on the choice of aspect ratio/wavenumber. This suggests that as $Ra \to \infty$, $Nu = c_n(k)Ra^{1/3}$ where $c_n(k)$ is the wavenumber dependent Chini-Cox prefactor [1]. It becomes more apparent that our calculations are consistent with classical 1/3 scaling of the Nusselt number when considering the right panel of Figure 7. This panel shows

the local exponent $\beta_n = \frac{d\log(Nu)}{d\log(Ra)}$ as a function of Ra. For all values of Γ, β_n eventually converges to $1/3$ for sufficiently large Ra-values. Over the considered range of Rayleigh numbers and data points collected, convergence occurred monotonically for $\Gamma \geq 0.2$. Convergence to the Chini-Cox prefactor occurred from below the final asymptotic value $c_n(k)$ whereas the local exponent converged to $1/3$ from above for all values of Γ. Overall, convergence to classical theory and the Chini-Cox prefactor is slower when the wavenumber $k = 2\pi/\Gamma$ is larger, requiring larger Ra-values for these solutions to exhibit asymptotic behavior.

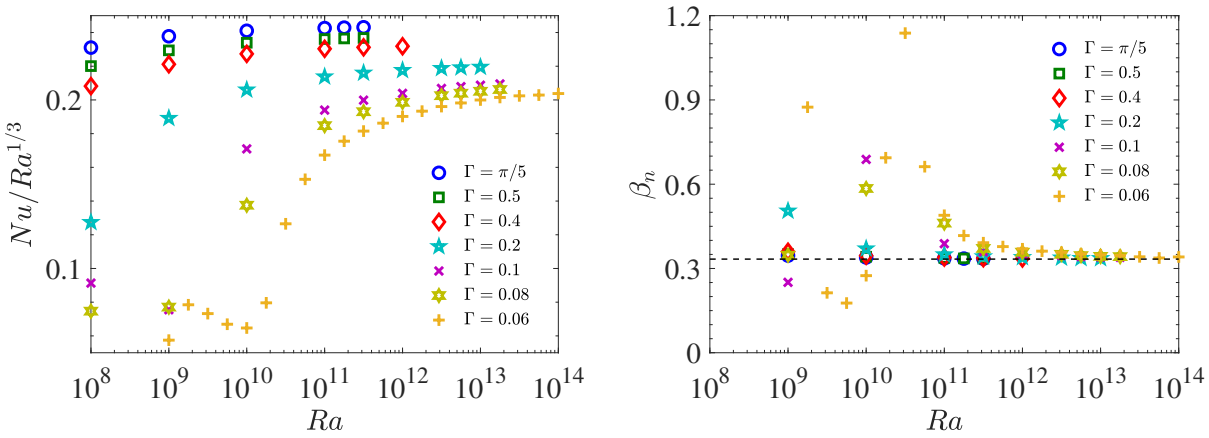

Figure 7: Left: Compensated plot of Nu vs. Ra for steady rolls on a semi-log plot with $Pr = 1$ over a variety of Γ. The horizontal trend for large Ra-values implies convergence to the Chini-Cox prefactor $c_n(k)$. Right: Finite difference approximation of the local exponent $\beta_n = \log(Nu_{i+1}/Nu_i)/\log(Ra_{i+1}/Ra_i)$ vs. Ra on a semi-log plot for steady rolls with $Pr = 1$ over a variety of Γ. A local exponent of $1/3$ is denoted by the dashed black line

The compensated Renolds number $RePr/Ra^{2/3}$ and the local exponent β_r as functions of Ra are given in Figure 8. Calculations for this figure were performed over the same range of Γ and Pr as Figure 7. The left panel of Figure 8 shows the relationship between $RePr/Ra^{2/3}$ and Ra. Our data shows the convergence of $RePr/Ra^{2/3}$ to different constants depending on the value of the aspect ratio/wavenumber. The convergence of this quantity implies $Re = c_r(k)Pr^{-1}Ra^{2/3}$ where $c_r(k)$ is the wavenumber dependent prefactor derived by Wen et al. [7]. The $2/3$ Ra-dependence of Re in the asymptotic regime is displayed more clearly in the right panel of Figure 8. This panel shows $\beta_r = \frac{d\log(Re)}{d\log(Ra)}$ as a function of Ra. The local exponent β_r eventually approaches $2/3$ for all values of Γ as $Ra \to \infty$. Over the considered range of Rayleigh numbers and data points collected, convergence to $c_n(k)$ and β_r occurred monotonically for $\Gamma \geq 0.08$. Convergence to $c_r(k)$ occurred from below the final asymptotic value whereas the local exponent converged to $2/3$ from above for all values of Γ. The fluctuations in the value of the prefactor $c_r(k)$ for each Γ were much less severe compared to $c_n(k)$ over the same range of Ra. This implies that Re reaches its asymptotic scaling much sooner than Nu does. Overall, convergence of Re to $Pr^{-1}Ra^{2/3}$-scaling is slower when the wavenumber $k = 2\pi/\Gamma$ is larger, requiring larger Ra-values for these solutions to exhibit asymptotic behavior.

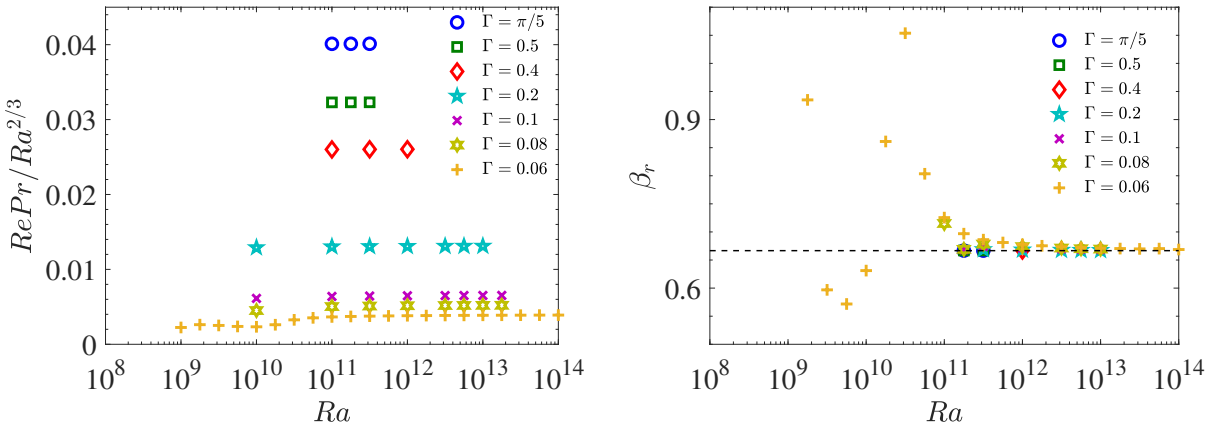

Figure 8: Left: Compensated plot of Re vs. Ra for steady rolls on a semi-log plot with $Pr = 1$ over a variety of Γ. The horizontal trend for large Ra-values implies convergence to the Chini-Cox prefactor $c_r(k)$. Right: Finite difference approximation of the local exponent $\beta_r = \log(Re_{i+1}/Re_i)/\log(Ra_{i+1}/Ra_i)$ vs. Ra on a semi-log plot for steady rolls with $Pr = 1$ over a variety of Γ. A local exponent of 2/3 is denoted by the black line.

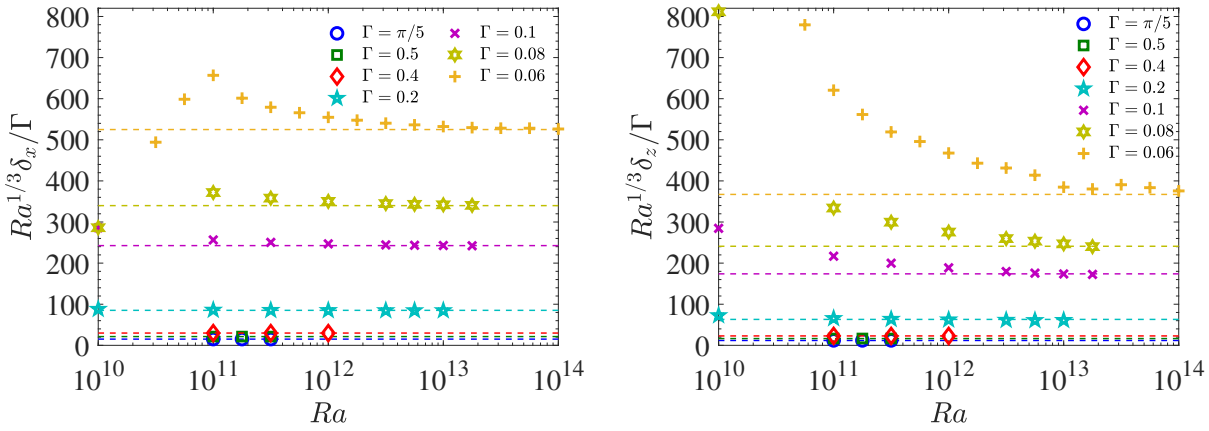

Figure 9: Left: Compensated vertical boundary layer thickness vs. Ra for steady rolls on a semi-log plot with $Pr = 1$ over a variety of Γ. Right: Compensated horizontal boundary layer thickness vs. Ra for steady rolls on a semi-log plot with $Pr = 1$ over the same range of Γ. The compensated vertical and horizontal boundary layers approach a constant for sufficiently large Ra-values as indicated by the dashed lines.

The left panel of Figure 9 represents the relationship between the thickness of the temperature's horizontal boundary layer and the Rayleigh number. The horizontal boundary layer thickness δ_x, defined as the width between the x-coordinate associated with the peak and the perimeter, was calculated by a cubic spline interpolation method. Our data suggest that as $Ra \to \infty$, $\delta_x \sim Ra^{-1/3}$ for all aspect ratios. This is illustrated by the convergence of $Ra^{1/3}\delta_x/\Gamma$ to different constants in the asymptotic regime of Ra. The constant of proportionality $C_{\delta x}$ relating δ_x/Γ and $Ra^{-1/3}$ is aspect-ratio-dependent, and data fitting to the last point of each set revealed the following relationship,

$$Ra^{1/3}\delta_x/\Gamma = 7.4798\Gamma^{-1.511} = C_{\delta x}(\Gamma) \quad \text{as} \quad Ra \to \infty. \tag{3.4}$$

These values, calculated by Eq. 3.4, are denoted by the dashed lines. The right panel of Figure 9 shows a similar relationship as the left panel but this time in the vertical direction. The vertical boundary layer

thickness δ_z is defined similarly as δ_x; the difference between the z-coordinate associated with the peak and the perimeter. The horizontal trend of the data for large Ra-values suggest that $\delta_z \sim Ra^{-1/3}$ as $Ra \to \infty$ for all considered Γ; however, δ_z takes much longer to converge to its asymptotic scaling than δ_x for all aspect ratios. As in the x-direction, the constant of proportionality between δ_z/Γ and $Ra^{-1/3}$, is aspect ratio dependent, and data fitting to the last point of each set revealed the following prediction of the asymptotic constant $C_{\delta z}(\Gamma)$ denoted by the dashed lines

$$Ra^{1/3}\delta_z/\Gamma = 5.9879\Gamma^{-1.463} = C_{\delta z}(\Gamma) \quad \text{as} \quad Ra \to \infty. \tag{3.5}$$

Interestingly, Eq. 3.4 and Eq. 3.5 follow similar but not identical Γ-scaling. A potential reason for this is that the x-direction reaches asymptotic scaling much sooner than the z-direction. Our data suggests that when $\delta_x/\Gamma \lesssim 0.02$ the value of $Ra^{1/3}\delta_x/\Gamma$ will be within 1% of $C_{\delta x}(\Gamma)$; however, to be within 1% of $C_{\delta z}(\Gamma)$, $\delta_z/\Gamma \lesssim 0.01$. The difference in the ratios indicates that larger Ra-values are required to obtain asymptotic scaling in the vertical direction than in the horizontal direction leaving convergence to a singular exponent a possibility for larger Ra-values.

4 Conclusions

Steady Rayleigh-Bénard convection between stress-free boundaries was studied via direct numerical simulation to calculate the local-maximum solution's properties and provide evidence for classical asymptotic scaling of the Nusselt and Reynolds number for fixed high-wavenumber. Properties of the aspect ratio that locally maximizes Nu, Γ^*_{loc} and fixed aspect ratios ranging from $0.06 \leq \Gamma \leq \pi/5$ were studied over moderate to large values of the Rayleigh number $10^8 \leq Ra \leq 10^{14}$ with fixed Prandtl number $Pr = 1$. Our results for Γ^*_{loc}, for the stress-free case, share many features with the no-slip case [6]. As in the no-slip case, our data suggest $Nu_{loc} = \mathcal{O}(Ra^{0.29})$, $Re_{loc} = \mathcal{O}(Ra^{2/5})$, and $k_{loc} = \mathcal{O}(Ra^{1/4})$ as $Ra \to \infty$. The interior of the temperature, stream function, and vorticity fields have an analytical solution given by Eq. 3.2 and have different properties than the fixed aspect ratio case, $\Gamma = 0.1$. Mainly, for $\Gamma = 0.1$, the temperature field develops an isothermal core, the stream function does not have multi-extremum properties, and the vorticity takes on a constant value of $\Psi_L \approx 67.36$ or $\Psi_R \approx -67.36$ for nearly all values left or right of $\Gamma/2$ respectively. For fixed aspect ratios $0.06 \leq \Gamma \leq \pi/5$ our data agrees with classical 1/3 Ra-scaling of the Nusselt number $Nu = \mathcal{O}(Ra^{1/3})$ [2] [3] and 2/3 Ra-scaling of the Reynolds number $Re = \mathcal{O}(Pr^{-1}Ra^{2/3})$ as $Ra \to \infty$. For each choice of aspect ratio, the quantities $Nu/Ra^{1/3}$ and $RePr/Ra^{2/3}$ approach a different constant suggesting a wavenumber/aspect ratio proportionality prefactor $c_n(k)$ [1] and $c_r(k)$ [7]. Convergence of Nu and Re to these asymptotic scalings takes longer for higher wavenumbers, and Re reaches its asymptotic scaling much sooner than Nu for all values of Γ. The slower convergence of higher wavenumber solutions makes sense in the context of the temperature boundary layer. We found that the thickness of the boundary layers δ_x and δ_z, defined as the distance between the peak value and the boundary, goes as $Ra^{-1/3}$, that is $\delta_x = \mathcal{O}(Ra^{-1/3})$ and $\delta_z = \mathcal{O}(Ra^{-1/3})$. Since classical scaling occurs when the width of the boundary layer is negligible compared to the size of the domain [1], larger Ra values are required for δ/Γ to become negligible when Γ is smaller. Potential future work includes improving Eq. 3.4 and Eq. 3.5 by constructing a more accurate upper-bound and obtaining data for new aspect ratios and higher Ra-number solutions for $\Gamma \leq 0.1$. Additionally, further investigating is needed to determine the Pr-dependence of high-wavenumber solutions.

Acknowledgements

I would like to thank Baole Wen for mentoring me though out this project and professor Charles Doering for allowing me to join his research group. Additionally I would like to thank the REU program for this amazing opportunity and for funding this project.

References

[1] Chini, G. P., and Cox, S. M. Large Rayleigh number thermal convection: Heat flux predictions and strongly nonlinear solutions. *Physics of Fluids 21* (2009).

[2] Malkus, W. V. R. The heat transport and spectrum of thermal turbulence. *Proc. R. Soc. Lond. Ser. A 225* (1954), 196–212.

[3] Priestly, C. H. B. Convection from a large horizontal surface. *Aust. J. Phys 7* (1954), 176–201.

[4] Spiegel, E. A. A generalization of the mixing-length theory of thermal convection. *Astrophys. J. 138* (1963), 216–225.

[5] Trefethen, L. N. Spectral methods in MATLAB. SIAM. (2000).

[6] Wen, B., Goluskin, D., and Doering, C. R. Steady Rayleigh–Bénard convection between no-slip boundaries. *Physics.flu-dyn.* (2020).

[7] Wen, B., Goluskin, D., LeDuc, M., Chini, G. P., and Doering, C. R. Steady Rayleigh–Bénard convection between stress-free boundaries. *Journal of Fluid Mechanics 905* (2020).